Metals & corrosion

Effect of temperature on the tensile deformation behavior and fracture mechanism of a transient liquid-phase bonding joint of γ′-strengthened Co-based single-crystal superalloy

S. Y. Wang[1,*], X. Y. Hou[1], Y. Cheng[1,2], Y. Sun[1,*], Y. H. Yang[1], J. G. Li[1], H. W. Zhang[1], and Y. Z. Zhou[1]

[1] Institute of Metal Research, Chinese Academy of Sciences, 72 Wenhua Road, Shenyang 110016, China
[2] School of Materials Science and Engineering, University of Science and Technology of China, 96, JinZhai Road, Hefei 230026, China

ABSTRACT

Tensile behavior at different deformation temperature of a transient liquid-phase (TLP) bonded joint of γ′-strengthened Co-based superalloy was investigated. A temperature dependence phenomenon of the joint's fracture position was found, which transferred from the base metal to the bonding area with increase in the temperature, and this is related to the deformation mechanism. At room temperature, dislocation shearing the γ′ phases in different areas of the joint domains the deformation and makes it heterogeneous, and more deformation has occurred at the BM because of lower content of γ′ phase, which makes the failure occurred at the BM. The deformation mechanism gradually transferred from dislocation shearing to bypassing the γ′ with increasing the temperature, making the deformation become diffused, and this can lead to the fracture of the joint's brittle borides, and the coalescence of the boride-induced cracks makes the fracture occur at the diffusion affect zone at 600 °C ~ 900 °C. As the secondary-γ′ in the joint's isothermal solidification zone dissolves at 1000 °C, more deformation occurs there and the accumulation of micro-voids induced by the dislocation climbing leads to the fracture.

Introduction

The γ'-strengthened Co-based superalloy has been widely concerned by many researchers since the discovery of the L1$_2$ structural Co$_3$(Al, W) compound [1]. Due to its higher melting temperature, oxidation, and wear resistance, it has the potential to become the next generation of superalloy [2–4]. However, limited welding researches have been carried out for the alloy, which is also a critical process performance concerned by many researchers. Therefore, conducting welding research is necessary and can accelerate the alloy to be put into use.

For the superalloys, which contain a higher amount of the Al, W, etc., adopting the fusion welding method is easy to form cracks due to their poor weldability [5]. The brazing method is often used in the superalloy components [6]. However, low-melting-point eutectics are easy to for in the brazing process, which makes the temperature-bearing capacity of the joint is insufficient. Therefore, the brazing method is usually used in the superalloy components, which do not need to withstand harsh temperatures [6, 7].

By contrast, the TLP bonding process has been proved to be an ideal joining method for superalloy, which has overcome the limitations of conventional fusion welding and brazing [8]. A typical TLP joint contains an isothermal solidification zone (ISZ) and a diffusion affect zone (DAZ) based on the microstructure [9–12]. Generally, the ISZ is free from the eutectics due to the isothermal solidification, while the DAZ contains many second phases due to the diffusion of melting point depressants (MPD) [13–15]. So far, for the Ni-based superalloy, researchers have carried out a large number of investigations on the microstructures of the TLP joint and found a lot of precipitates [16, 17]. The microstructure characteristics of a TLP joint is now well defined.

However, the mechanical property of the TLP joint is always the most concerning problem by researchers, which is also an important index to evaluate the success or failure of a TLP joint. The mechanical properties of a TLP joint are directly related to the microstructure, which can be directly affected by the bonding process. For this, researchers have carried out lots of investigations on the effect of the bonding parameters on the microstructure and mechanical properties. Farzam. et al. [18] investigated the effect of bonding time on mechanical properties of a TLP bonded IN-939 joint. He found that increasing the bonding time can decrease the brittle centerline eutectics and raise the content of the solid solution strengthening elements in the center of the joint, which makes the shear strength increase significantly. Alireza et al. [19] studied the effect of the bonding temperature and found that increasing the temperature would lead to a more uniform joint and improve the mechanical properties. Danesh et al. [20] found similar results. However, they also pointed out increasing the temperature to a certain point would make the eutectics in the joint reappear and lower the corresponding shear strength. Such results have also been reported by other researchers [11]. It can be seen that researchers have reached a broad consensus on the relationship between the bonding parameters and joint performance.

Nevertheless, only understanding the relationship between the bonding parameters and the joint performance is not enough to further improve joining quality. The deformation mechanism and fracture behavior of the TLP bonded joint need to be investigated. More importantly, a TLP joint contains different zones (ISZ, DAZ, and BM), and the deformation mechanism between each zone could be different. So far, the relevant studies about this are very limited. As is known, during the loading process, as the weakest point of a joint determines the strength, investigating the deformation behavior of each zone helps to determine the crack-initiation site and understand the failure mechanism of the joint. Therefore, it is significant to carry out the relevant research. Besides, most of the current studies focus on the fracture behavior of the TLP joint at one loading condition (room or high temperature). Few researchers comprehensively consider the fracture behavior of the joint at different deformation temperatures, which can more fully evaluate the performance of the TLP joint.

For the γ'-strengthened cobalt-based single-crystal superalloy, as there are not any commercial filler alloys for TLP bonding, we designed a Ni-based filler alloy (Ni–Cr–W–B) based on the thought of high-matched joint of the fusion welding [21] to improve the high-temperature mechanical properties. Our previous research has proved that the TLP joint's bonding area can precipitate the γ' (Ni$_3$Al) phases

[22], but the mechanical behavior is still not entirely clear.

Accordingly, this paper aims to determine the fracture mechanisms of different zones in the TLP joint at different loading temperatures and the corresponding fracture behaviors. Our studies will provide the theoretical basis and a reference value for the TLP bonding and repairing of the γ′-strengthened Co-based single-crystal superalloy in the future.

Experiments

The γ′-strengthened Co-based single-crystal superalloy [23], developed by Institute of Metal Research, Chinese Academy of Sciences, was utilized as the base metal (BM). The filler alloy powder (Ni–Cr–W–B) was prepared by powder metallurgy technology. The compositions of the BM and filler alloy are listed in Table 1.

As the main stress direction of the single-crystal superalloy parts is [001] in the practical engineering applications, we choose this as the bonding direction, and the as-cast Co-based single-crystal BM rod with a diameter of ∼ 15 mm was directionally solidified along [001], and the deviation of the rods from [001] direction was controlled by less than 10 degrees. The phase constitution of the as-cast BM is γ/γ′ and some compounds, which are rich in W and Ta and distribute in the interdendritic area (Fig. 1a∼b), and these compounds are inferred to be the Co_3Ta according to their chemical composition (Fig. 1a). Before bonding, the BM was subjected to a solid solution heat treatment (according to Ref [24]). After the heat treatment (1280 °C/5 h), the BM become more uniform and the Co_3Ta are removed, and the BM only contains the γ and γ′ phases (Fig. 1c∼d). The heat-treated BM was cut into two parts (vertical to [001]), which were then in situ bonded to exclude the influence of orientation on the deformation behavior of the joint. A sandwich-like specimen was assembled (see the schematic of "Bonding sample" in Fig. 2), and the specimen was heated to 1220 °C at the rising rate of 20 °C/min under a vacuum of

5×10^{-3} Pa, and held for 4 h. Finally, the specimen was cooled down to room temperature in the furnace. The gap size was controlled by a nickel wire (Φ100 μm). After bonding, the sample was subjected to a double-aging treatment (1000 °C/36 h + 750 °C/24 h).

Tensile tests were performed on an AG 250 electronic tensile testing machine at 20 °C, 600 °C, 800 °C, 900 °C, and 1000 °C, respectively, at a constant crosshead separation rate of 0.1 mm/min. The specimen configuration for the tensile test is shown in Fig. 2. For every deformation temperature, two tensile conditions were performed: one was stretching the specimen to fracture to analyze the tensile properties of the sample (yield strength, ultimate strength, and elongation), and the other was stretching the specimen at the point which is just before the fracture (this is based on the previous stretching to fracture test). The schematic of the tensile test is illustrated in Fig. 2. The COMSOL Multiphysics software was used to simulate the stress field of the TLP joint under the tensile stress. We selected the solid mechanics module and built a two-dimension model (Fig. 19) according to the cross section of the TLP joint (Fig. 3a). We built a 1300 μm × 500 μm two-dimension model according to the TLP joint, and the "Superfine mesh" is selected. The wide of ISZ is 100 μm and the DAZ (the length of the boride) is 200 μm. We make the following assumption: the BM and the ISZ are a single-phase solid and the matrix of the DAZ is same as the BM; the shape and size of all the borides are the same, which is assumed to be a antiparallelogram, and the vertices are chamfered to avoid non-convergence; the boride induced crack (BIC) is assumed to be a ellipse ($a = 5$ μm, $b = 18$ μm); the parameters of the ISZ, DAZ, and BM are listed in Table 2.

Microstructures of the TLP joint and the fracture were analyzed by a Cambridge-S360 scanning electron microscope (SEM). The deformation microstructure was analyzed by a JEOL 2100F transmission electron microscope (TEM). The SEM samples were polished and etched with a solution of $CuSO_4/HCl/C_2H_4OH$. The interrupted tensile

Table 1 Compositions of the base metal and Ni–Cr–W–B powder (wt%)

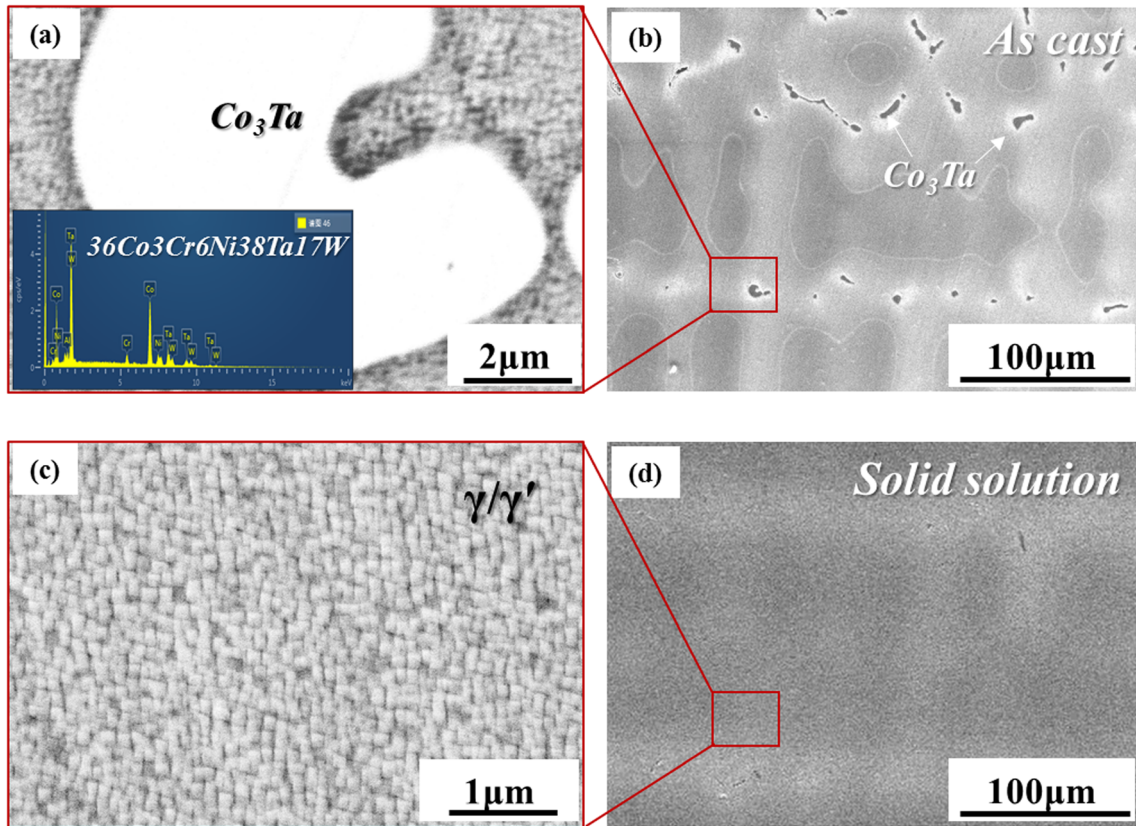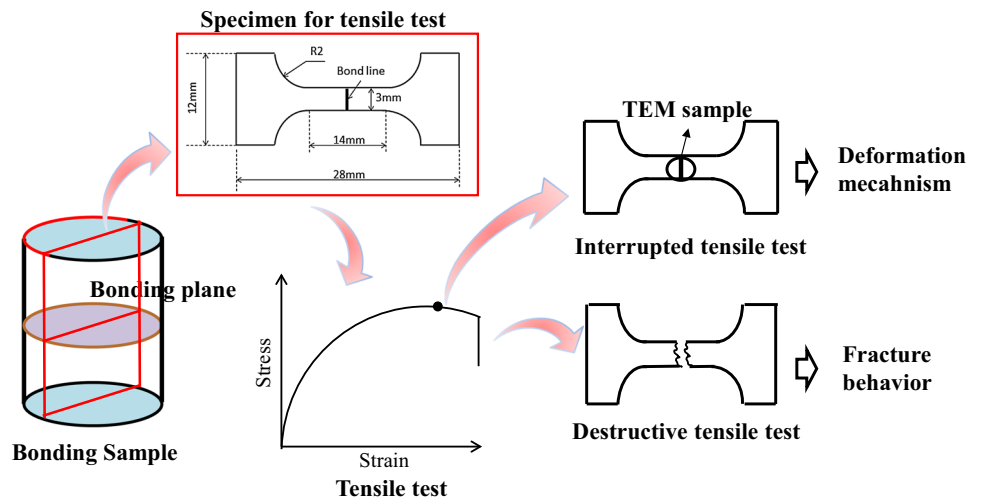| Material	Ni	Cr	W	Al	Ta	Co	B
Base metal	13–15	3–5	13–15	4–6	7–9	Bal	< 0.1
Filler alloy	Bal	13–15	6–8	< 0.1	< 0.1	< 0.1	3–5

Figure 1 Microstructure of the as-cast BM **a**–**b** and solid solution treated BM **c**–**d**.

Figure 2 Schematic diagram showing the tensile specimen preparation method.

samples were mechanically ground to less than 50 μm. Then, the samples were punched into a Φ3 mm thin slice. A Leica multifunctional ion etching instrument was used to etch the ISZ, DAZ, and BM of the samples to ensure that the thin-region fell in the desired positions.

Results

Microstructure of the joint

Figure 3 shows the microstructure of the TLP joint. The ISZ is composed of the γ'/γ phases, and there are
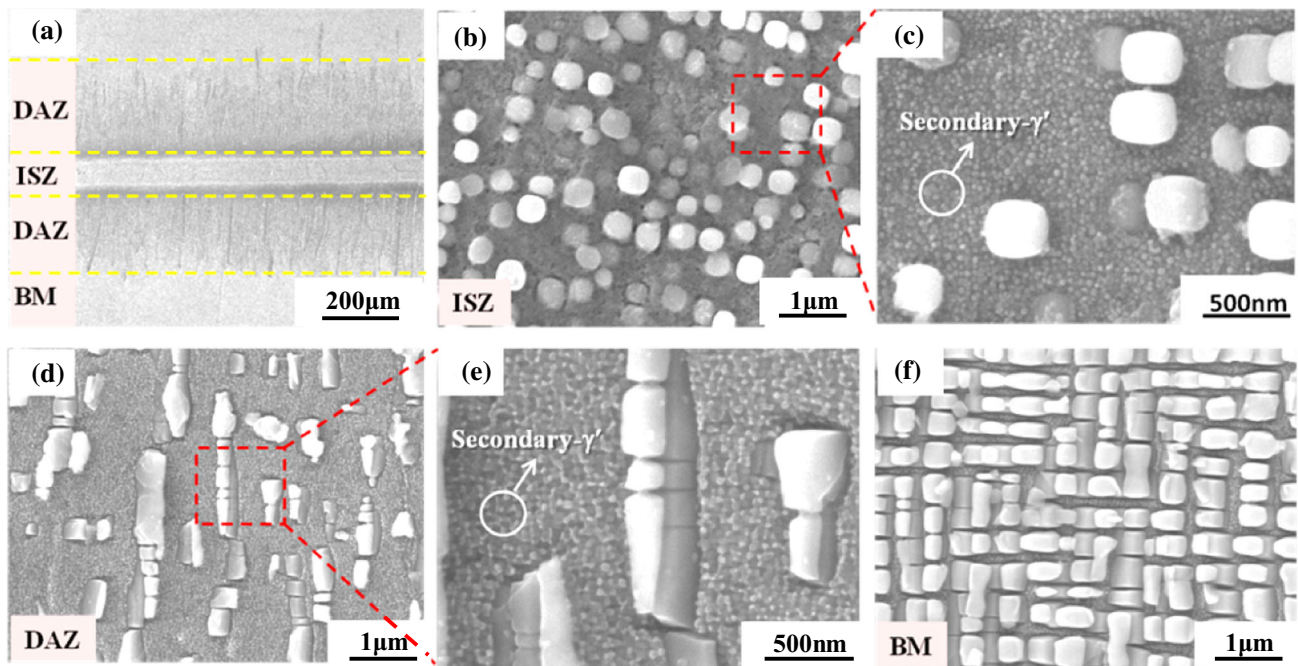
Figure 3 SEM images showing the microstructure of different areas of the TLP joint after bonding and heat treatment. **a** Overview of the TLP joint; **b**–**c** ISZ; **d**–**e** DAZ; **f** BM.

many secondary-γ' precipitated in the γ' channel (Fig. 3b$\sim$c). In addition to the γ'/γ phases, the DAZ contains many borides (Fig. 3a and d), which makes the DAZ has the higher harness than that of the BM and ISZ [22]. The γ' phases (refer to primary-γ' phases in the following discussion) exhibit chamfered cuboidal and cuboidal morphology in ISZ and BM, respectively. The morphology of γ' phases in the DAZ (between the borides) is more complex compared with that of the ISZ-γ' and BM-γ' (Fig. 3f), and rafting γ' phases and irregular γ' phases can be observed (Fig. 3d$\sim$e).

Figure 5 illustrates the mathematical statistic results of the γ' phases. The size distributions of the γ' phases in different areas are close to the Gaussian distribution (Fig. 5a$\sim$c). The DAZ-γ' phases have a wider equivalent size range and higher standard deviation (Fig. 5e), which are discussed in Ref. [22]. The average sizes of the γ' in the three areas are close to each other ($\sim$ 200 nm). However, the volume fractions of the γ' in ISZ and DAZ are lower than that of the BM (Fig. 5f), which is due to the lower content of γ' forming elements Al in these areas (see Fig. 4).

Tensile properties

Figure 6a shows the engineering stress–strain curves. The joints exhibit different tensile behavior in various temperatures. From the room temperature (20 °C, RT) to 600 °C, a relatively weak work-hardening phenomenon can be observed. From 800 °C to 900 °C, the work-hardening phenomenon becomes stronger. At 1000 °C, no strain-hardening effect occurred.

Figure 6b shows the yield strength and elongation. The yield strengths of the TLP joint are closer to that of the BM at different temperatures. Like the BM, the TLP joint exhibits a three-stage temperature dependence of stress. In the low-temperature range (RT $\sim$ 600 °C), the yield strength decreases with temperature. From 600 °C to 800 °C, abnormal yield behavior can be found. When the deformation temperature is above 800 °C, the yield strength decreases rapidly with increase in the temperature. In addition to the RT elongation, which is closer to that of the BM, the elongation of the joint is much lower than that of the BM. Besides, the elongation of the TLP joint decreases with the increase in deformation temperature. However, it enjoys a slight increase when the deformation is above 900 °C.

Table 2 The material properties parameters used in the finite element analysis

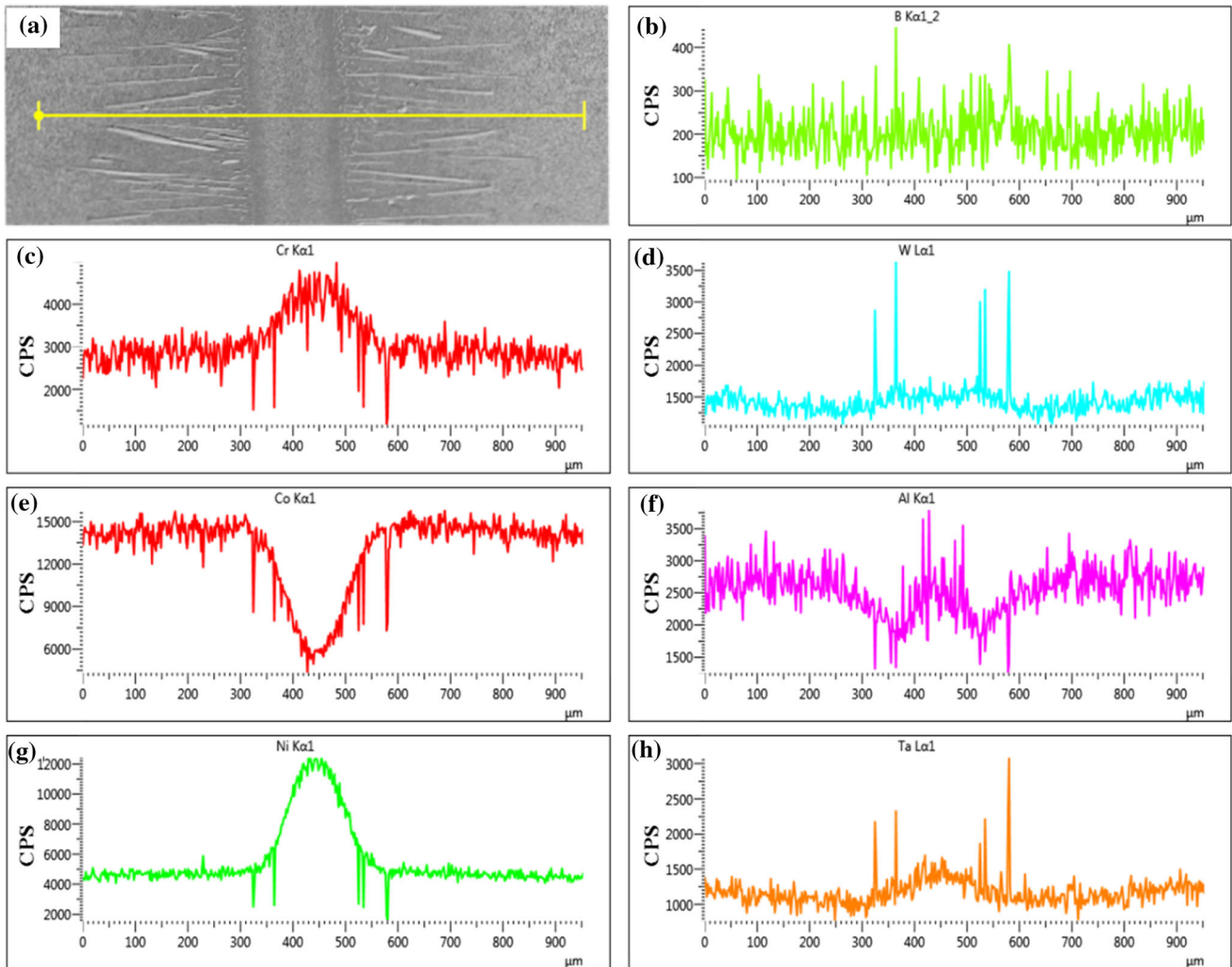| Temperature material property	Low temperature Young modulus (GPa)	High temperature	Low temperature Poisson's ratio	High temperature
ISZ	88.3	69.6	0.356	0.356
DAZ/BM	80.5	75.6	0.38	0.38
Boride	441	441	0.26	0.26

Figure 4 EDS line scan across the bond region to show the elements distribution. **a** SEM image; **b** B; **c** Cr; **d** W; **e** Co; **f** Al; **g** Ni; **h** Ta.

Deformation substructures

Low temperature (20 °C∼600 °C)

Figure 7 shows interrupted deformation substructure at RT. In the ISZ (Fig. 7a∼b), a long straight slip line can be observed at some points (Fig. 7b), which shears both the γ and γ′ phases, and the direction of the slip line is along < 110 > of the matrix. Few dislocations can be observed between the slip line, and the substructure resembles the as-received material (Fig. 7a). The slip in the dislocation plane domains the deformation at ISZ at RT. In the DAZ (Fig. 7c∼d), few dislocations can be observed near the boride
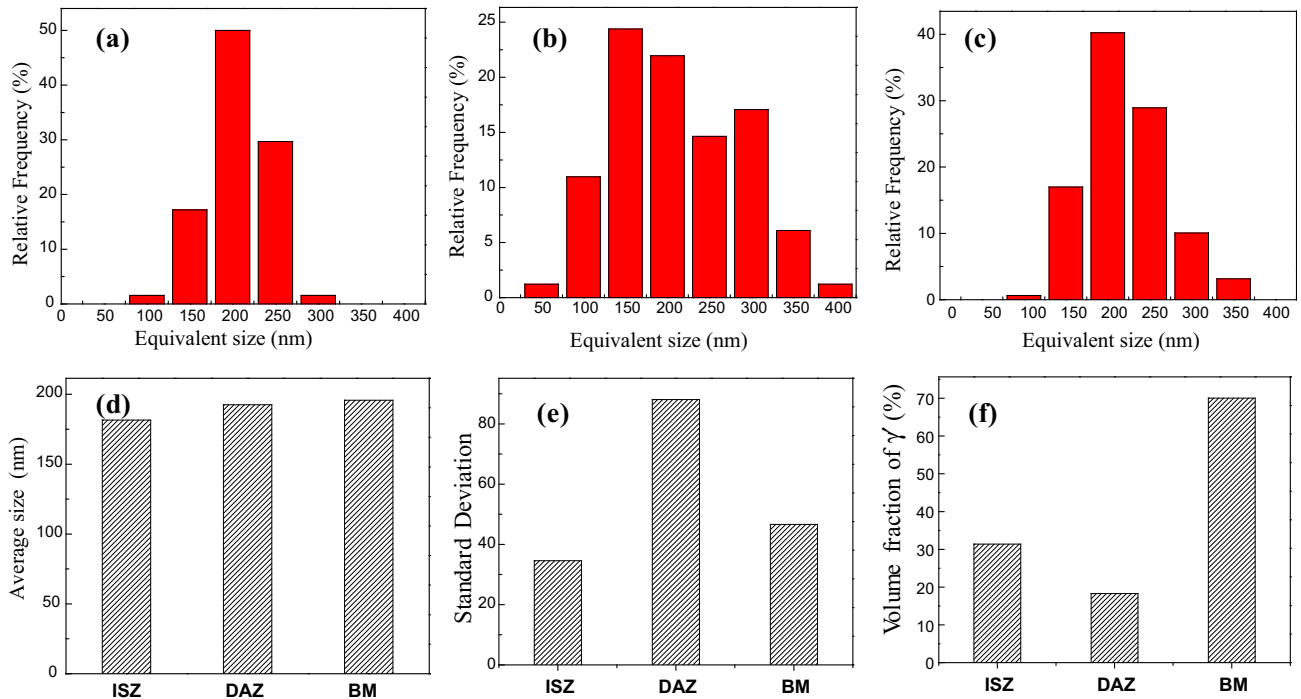
Figure 5 Mathematical statistics results of the γ' precipitate after double-aging treatment. Relative frequency of the equivalent size of γ' precipitate in **a** ISZ, **b** DAZ, **c** BM; **d** Average size; **e** Standard deviation; **f** Volume fraction of γ' phases (area fraction measured in the 2D SEM image).
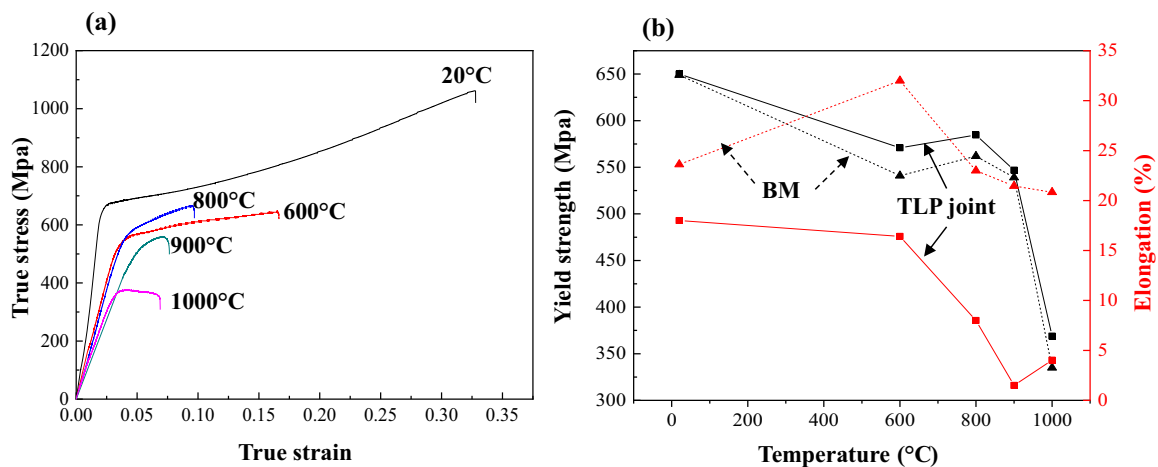

Figure 6 Tensile behavior of the TLP joint at different deformation temperatures. **a** True strain–stress curves; **b** Temperature dependence of the 0.2% yield strength and elongation. The black dot line represents the yield strength of the base metal (BM).

(Fig. 7c), and a/2 <011> dislocation pairs shearing the γ' phases can be observed at the position where it is relatively far away from the boride (see the inserted image in Fig. 7c). There are also exceptions, in some areas of the DAZ, more dislocations and long slip lines can be found near a boride, and the long slip lines are originated from the boride (Fig. 7d). In the BM, dislocations shearing the γ' phase is the main deformation mode. Some stacking fault (SF) loops can be observed in γ' phases (Fig. 7f), which is often observed in the Ni-based superalloy deformed at low temperature and is believed to be the result of local

Figure 7 TEM images showing the deformation microstructures of the ISZ, DAZ, and BM of the TLP joint tested at room temperature. **a~b** ISZ; **c~d** DAZ; **e~f** BM; **e** The area near the joint (NJ); **f1~f2** The area away from the joint (AFJ).
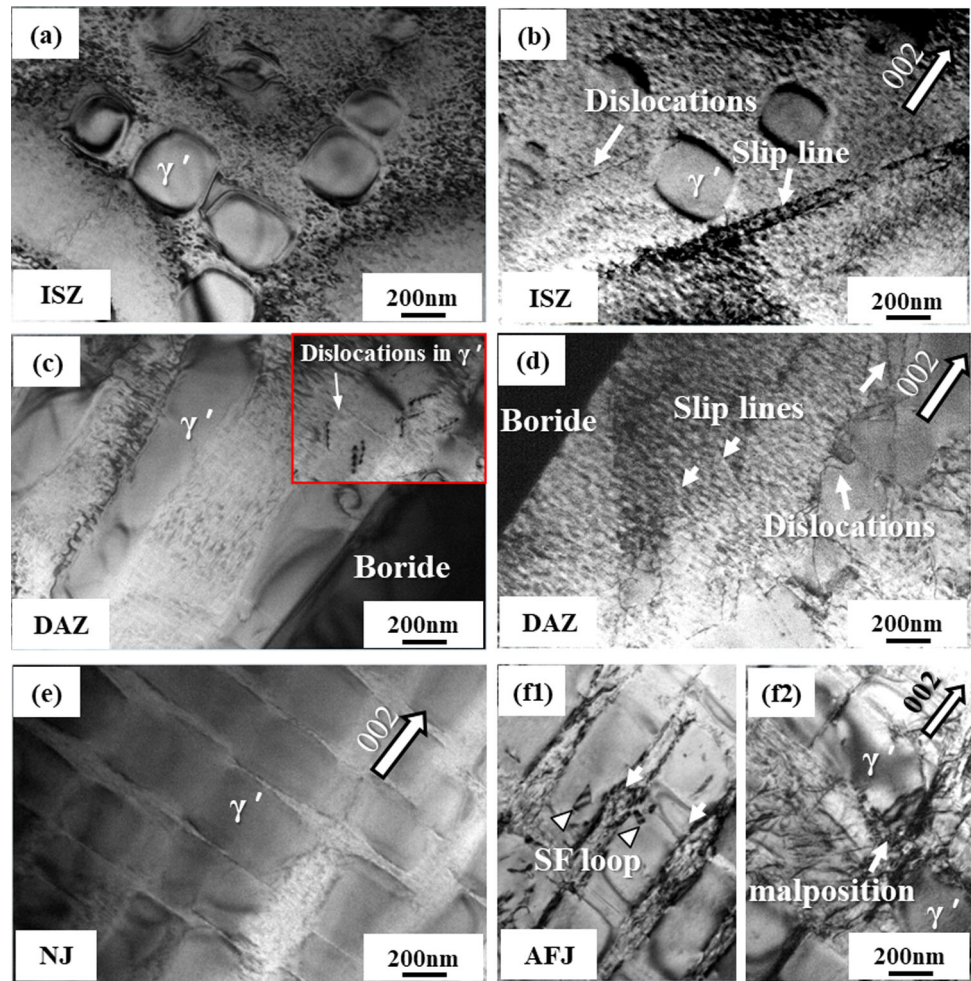
alloy elements segregation [25]. Fewer dislocations can be observed in the area near the joint than the area away from the joint, which coincides with the bamboo-like morphology of the joint (see Fig. 12 in Sect. 3.4). This proves the uneven deformation between the bonding area and the BM.

Figure 8 shows the 600 °C deformation substructures. The substructures are similar to that of the RT. Long slip lines shearing the γ′ and γ substrate can also be observed in the ISZ (Fig. 8a). The deformation of the position swept by the slip line is large, and some γ′ phases are broken by the slip of dislocations. Between the slip lines, there are few dislocations. In the γ channel, the a/2 <011> dislocations shearing the secondary γ′ phases (S-γ′) can be observed (Fig. 8b). In the DAZ, the dislocation density is still very low near the boride (Fig. 8c), and the a/2 <011> dislocation pairs shearing the γ′ phases can also be observed between the borides (Fig. 8d). In the BM, there are also many slip lines, which are

more than that of the ISZ. The dislocation density away from the joint is higher than that near the joint (Fig. 8e~f).

Intermediate temperature (800 °C~900 °C)

Figures 9 and 10 illustrate the deformation substructures of the joint tested at 800 °C and 900 °C, respectively. At 800 °C, the S-γ′ phase in the γ channel shows a partially dissolved morphology, and dislocations bowing in the γ channel of the ISZ can be observed (see the black arrow in Fig. 9a). Dislocations pile-up around a γ′ phase can also be observed (see the triangular symbol in Fig. 9a). In some γ′ phases, a sharp planar fault can be observed, and the propagation direction of the faults in the two-dimension image is <011> (Fig. 9a, marked with a white arrow). When tilting the specimen, the fault gradually presents the typical stack fault morphology (see the inserted image in Fig. 9a). This means the a/

Figure 8 Deformation substructures of the TLP joint tested at 600 °C. **a~b** ISZ; **c~d** DAZ; **e~f** BM; **e** The area near the joint (NJ); **f** The area away from the joint (AFJ).
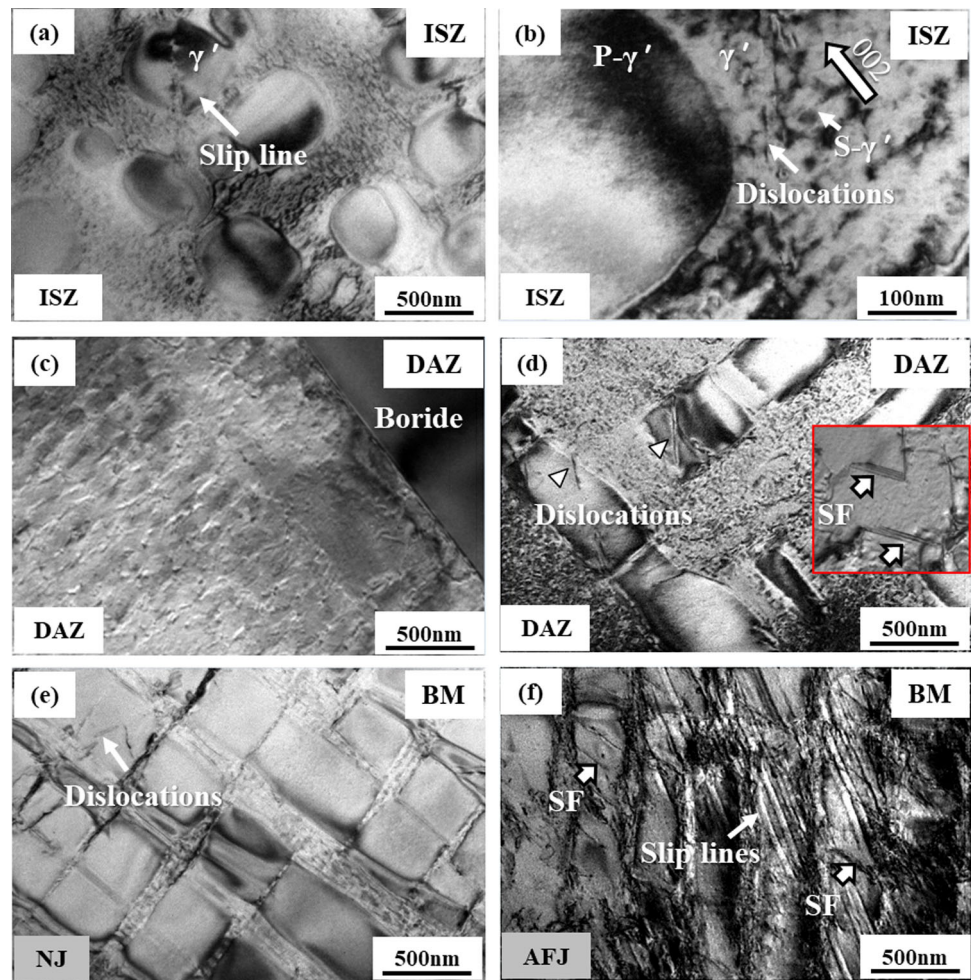

2 <011> dislocations in the γ channel could decompose and form the leading a/3 <112> partial dislocations [25] in the γ′ phases. Besides, there are also a few dislocation pairs in the γ′ phases (Fig. 9b). In the DAZ, dislocations cross-slip can often be observed in the γ channel (Fig. 9c and d). In some parts of the γ channel, some dislocations tangle together. It has been reported that this kind of dislocation is a 60° mixed dislocation that crosses slip from (1$\bar{1}$1) plane to (111) plane [26]. Also, the dislocation pairs and SF loops can be observed in the γ′ phase (Fig. 8d). In the BM, partial dislocations shearing the γ′ phases and leaving the SFs in them is the main deformation mechanism (Fig. 9e and f).

At 900 °C, the S-γ′ phases in the γ channel are totally dissolved, many curved dislocations can be observed both in the γ channel and γ′ phases, and dislocation pairs shearing the γ′ phases is the general features of the ISZ (Fig. 10a). This alludes to the deformation mechanism of a/2 <011> dislocations

bypassing and a <011> superdislocations shearing the γ′ phases in the ISZ. Besides, it is interesting to find many wavy dislocations leaving on the margin of γ′ phases (Fig. 10b). Such configuration has been demonstrated to be the result of dislocation gliding and climbing the γ′ phase [27]. In the DAZ, dislocations bypassing the γ′ phases are prevalent even beside a perfect boride (Fig. 10c). However, SFs can be observed at the position closer to the BM. In fact, in our observation process, such deformation behavior also exists in the 800 °C-deformed substructure.

This is easy to understand because the closer the BM in the DAZ, the more similar the microstructure is to the BM [24]. Therefore, the deformation behavior should be similar. In the BM, many SFs can be observed in the γ′ phases. Meanwhile, dislocation bowing in the γ channel can also be observed, but this phenomenon is not prevalent. This indicates that the deformation mechanism of BM is mainly caused by

Figure 9 TEM images showing the deformation substructure of the TLP joint tested at 800 °C. **a∼b** ISZ; **c∼d** DAZ; **e∼f** BM.
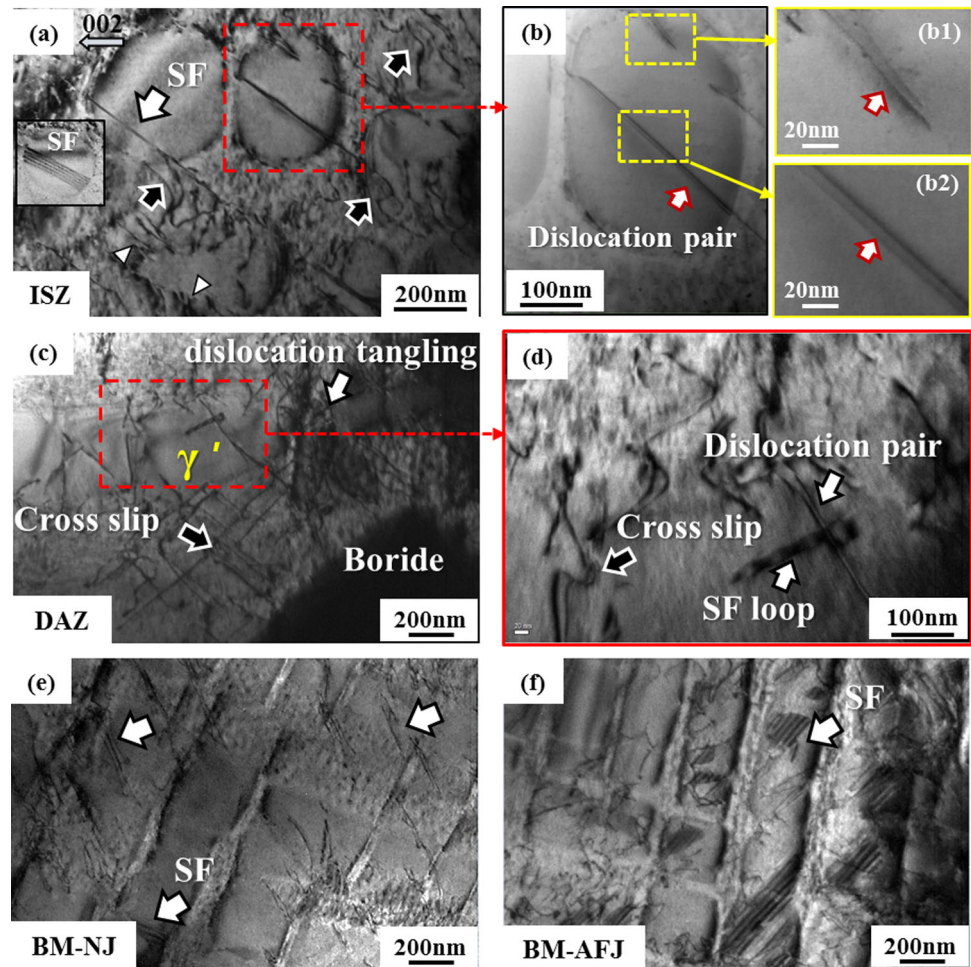
the partial dislocation shearing the γ′ phase. In general, the dislocation density of the BM near the joint at the intermediate temperature range is significantly higher than that at low temperatures.

High temperature (1000 °C)

Figures 11 illustrates the 1000 °C deformation substructure. Many curved dislocations can be observed in the ISZ (Fig. 11a, b, and d), indicating the Orowan bypassing deformation mechanism. Some irregular dislocation nets can be observed at the γ/γ′ boundary (Fig. 11a). Meanwhile, many arc-shaped dislocations can be found in the γ′ phases. Their morphology is not a/3 <211> partial dislocation, usually straight and short. Some of the dislocations are in pairs, and others are single. The arc-shaped dislocations are identified according to the $g \cdot R = 0$ invisibility criterion. It can be seen that the dislocations are visible when $g = 002$ and invisible when $g = 020$ (Fig. 11b and d), so the dislocation pair is

a <101> superdislocation and the single dislocation is a/2 <101> superdislocation partial leaving an APB in the γ′ phase. The schematic of the dislocations is illustrated in Fig. 11c.

Figure 11e∼h illustrate the deformation substructures of the DAZ and BM. The deformation mechanism of the DAZ and BM is similar to that of the ISZ, and the dislocations bypassing and shearing the γ′ phases domains the deformation. The dislocation density in different areas of the TLP joint is closer, indicating a more uniform deformation than the low-temperature. In addition, tangled or blocked dislocations are rarely observed at this deformation temperature, which makes it easier for the dislocations to move. Therefore, there is no work hardening phenomenon at 1000 °C (Fig. 6).

Fracture behavior

Figure 12 shows the SEM images of the TLP joint after fracture at RT. The fracture occurs at the BM,

Figure 10 TEM images showing the deformation substructure of the TLP joint tested at 900 °C. **a**∼**b** ISZ; **c**∼**d** DAZ; **e**∼**f** BM.
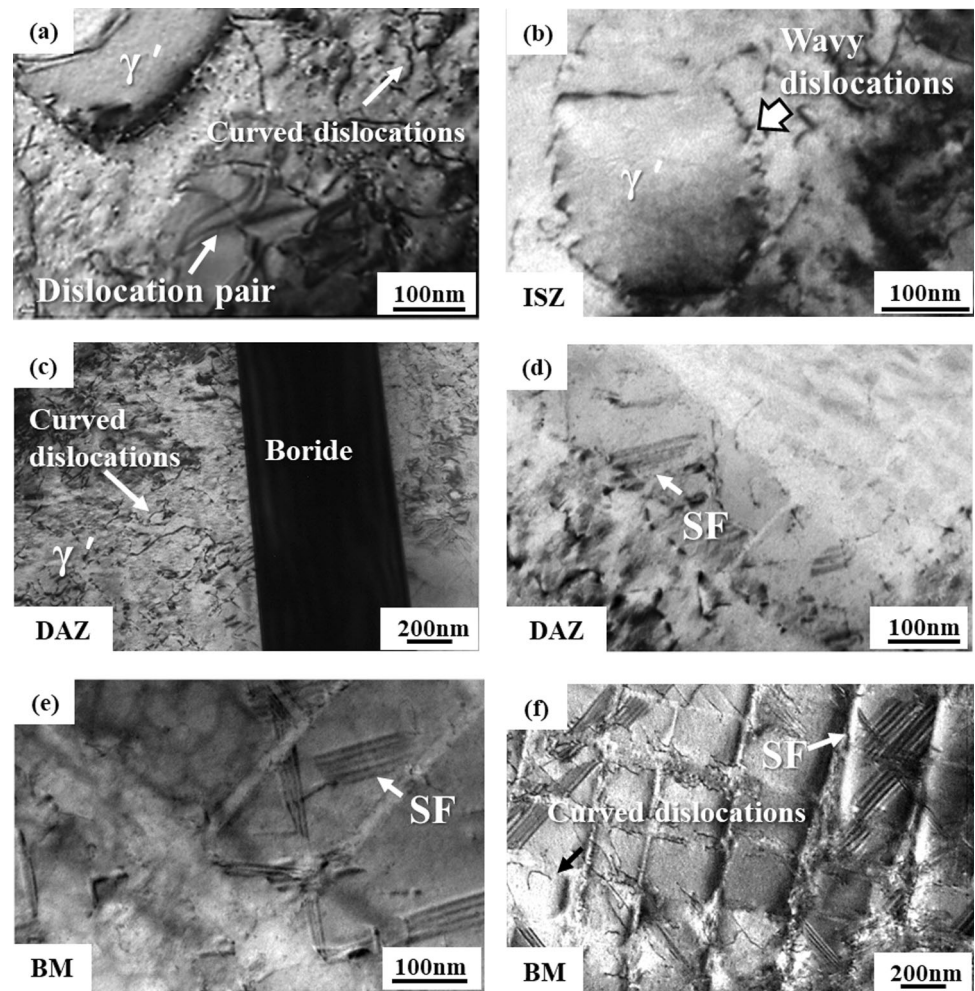

away from the TLP joint. The bonding area looks like a bamboo-joint (see the enlarged image in Fig. 12a), which means a larger deformation has occurred in the BM than in the TLP joint. Slip lines can be observed in the area away from the joint, which almost cross the two edges of the BM (Fig. 12a). Boride-induced cracks (BICs) can be seen in DAZ, but they do not lead to the failure of the joint. In some parts of the ISZ, slip lines can also be observed. However, these slip lines do not go through the entire bonding area, which end up at the interface of ISZ/DAZ, which means dislocations are harder to slip across the DAZ. The slip lines are consistent with the substructures illustrated in Fig. 7.

Figure 13 shows the fracture paths of the specimens tested at 600 °C∼900 °C. All the tested samples fail at the DAZ and many BICs can be found beside the paths (Fig. 13d∼f). However, it is interesting to find the fracture paths located at different DAZ

positions with different temperatures. To quantify the position, we measured the length between the fracture path and the interface of DAZ/ISZ on each specimen. A relative position of the fracture path is defined as L/D, where L represents the length between the fracture path and the interface of DAZ/ISZ, and D represents the thickness of DAZ.

Figure 14 illustrates statistical results. The relative position first increases slightly, then decreases dramatically, and reaches a peak at 800 °C (Fig. 14a). Such a result is not accidental, and it can be observed by repeated experiments. Besides, we also measured the opening displacement of BICs beside the fracture path and found the variation trend of crack opening displacement (COD) with temperature is opposite to the relative position (Fig. 14b), and there is a certain correlation between the two physical quantities (Fig. 14c).

Figure 11 TEM images showing the deformation substructure of TLP joint tested at 1000 °C. **a**, **b**, **d** ISZ; **c** Schematic of the dislocations in the ISZ-γ′ phase; **e ∼ f** DAZ; **g** Near joint zone of the BM; **h** Away from the joint zone of BM.
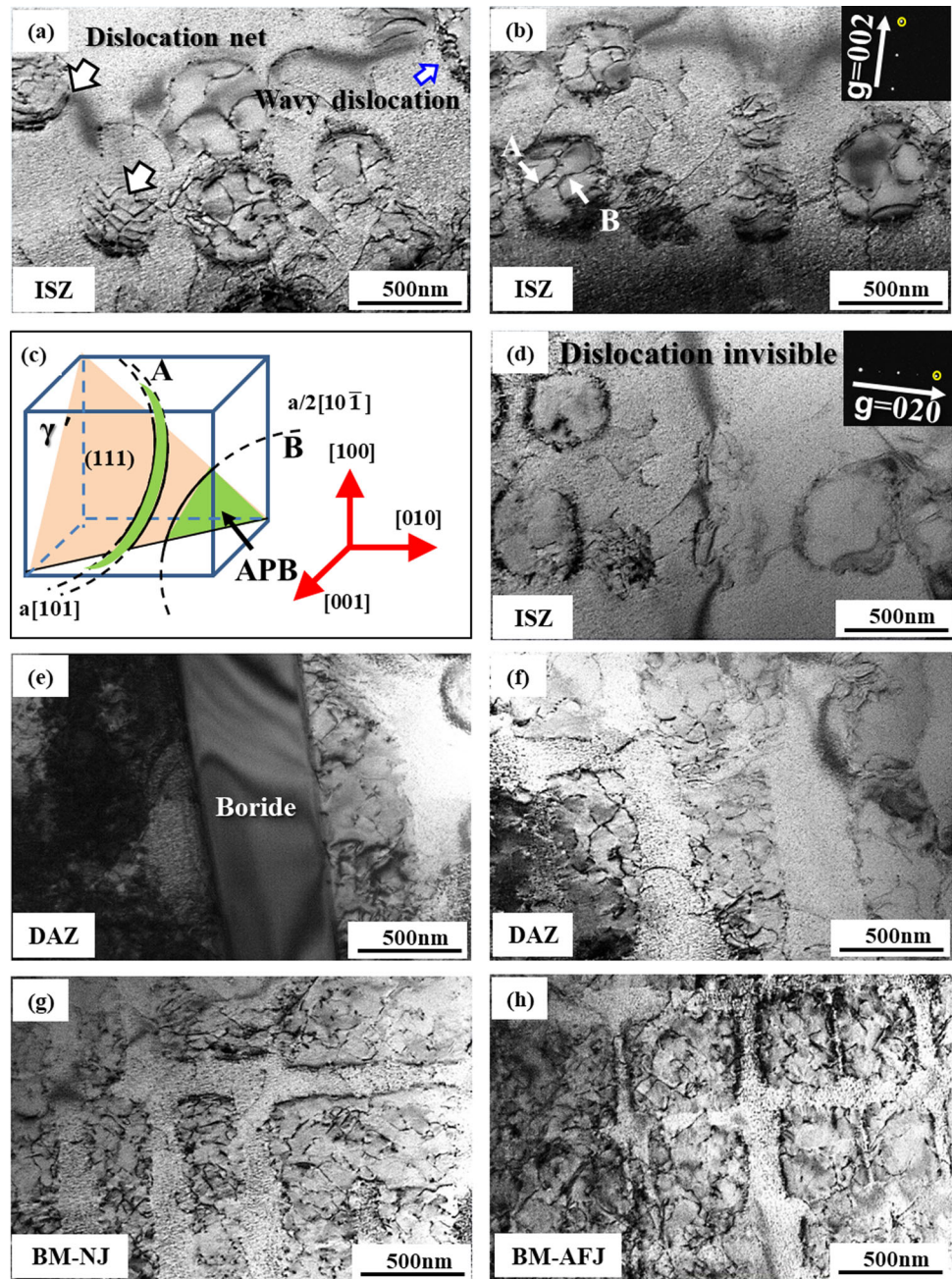
At 1000 °C, fracture occurs at ISZ (Fig. 15a). The BIC can also be found in the DAZ (Fig. 15d) and the COD is obviously larger than that of the 600 °C ∼ 900 °C, but they do not lead to the failure of the joint. The necking phenomenon can be observed at the margin of the specimen (Fig. 15b). In the ISZ, cracks prefer to locate at the sub-grain boundaries (SB in Fig. 15e), which are the TLP bonding defects. Most sub-grain boundaries are vertical to the loading direction (Fig. 15c and f).

Figure 16 shows fracture surfaces of the TLP joints tested at 600 °C ∼ 900 °C. The surfaces are relatively flat and the morphologies show a brittleness character. Many acicular-like pits induced by the DAZ borides can be observed in all the samples. An obvious crack propagation surface can be observed at the edge of each boride pit. Figure 17 shows the fracture surface tested at 1000 °C. The fracture surface is cavernous. Two morphologies can be observed, which are divided by a yellow dotted line

Figure 12 SEM images showing the macrostructure and microstructure of the TLP joint after fracture at room temperature. **a** Macrostructure of the tensile test specimen showing the rupture location and morphology of the bonding area; **b** Microstructure of the joint showing the **b** DAZ and **c** ISZ.
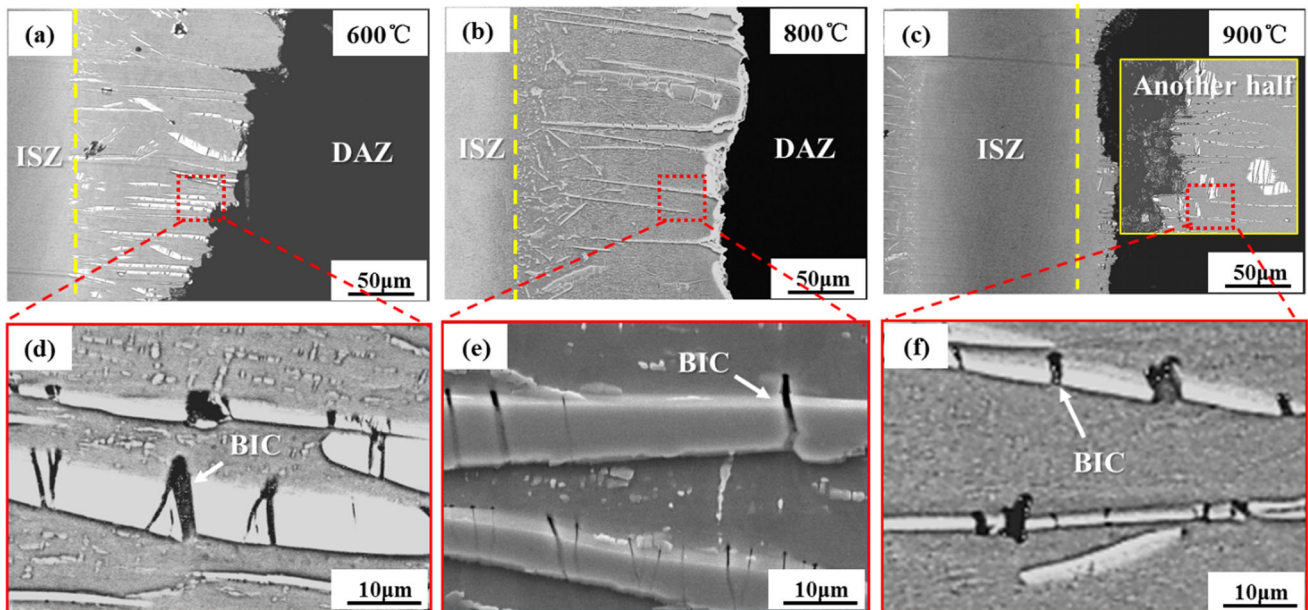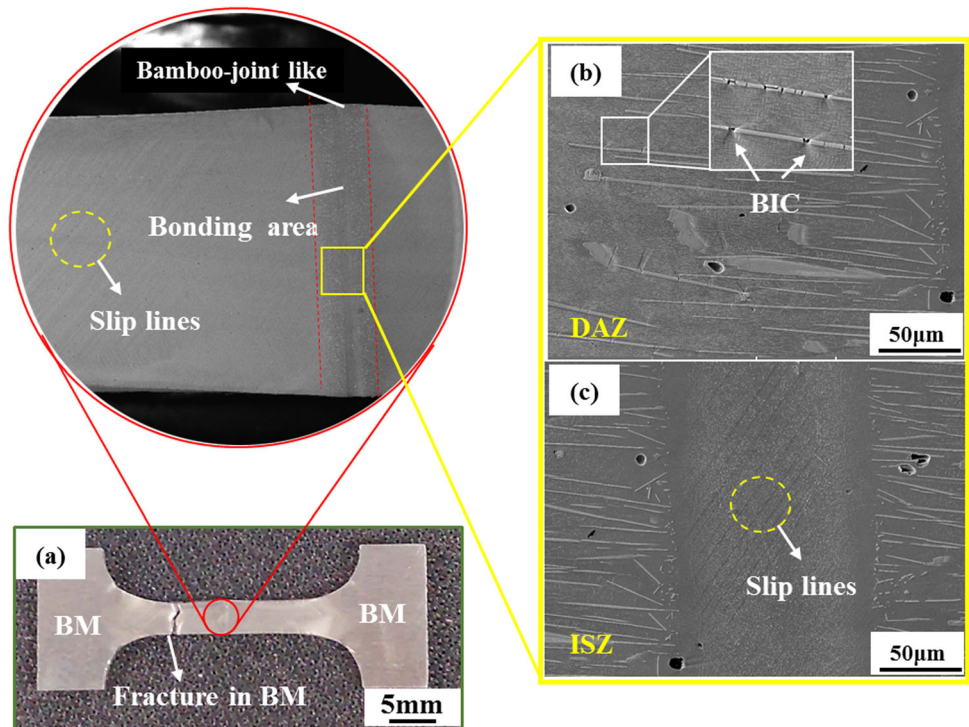

Figure 13 SEM images showing the fracture path of the specimens tested at the temperature range of 600 °C ∼ 900 °C. **a, d** 600 °C; **b, e** 800 °C; **c, f** 900 °C.

(areas A and B in Fig. 17a). Area A has some relatively small holes (hole A), where it shows the ductile fracture morphology. Area B has some bigger holes (hole B), and the surface is relatively smooth. An obvious flat crack propagation plane can be found around hole B. A torn edge can be observed at the edge of each crack propagation plane (Fig. 17c). In some areas of area B, the intergranular fracture morphology can be observed, corresponding to the sub-grain boundary cracks described in Fig. 15e.
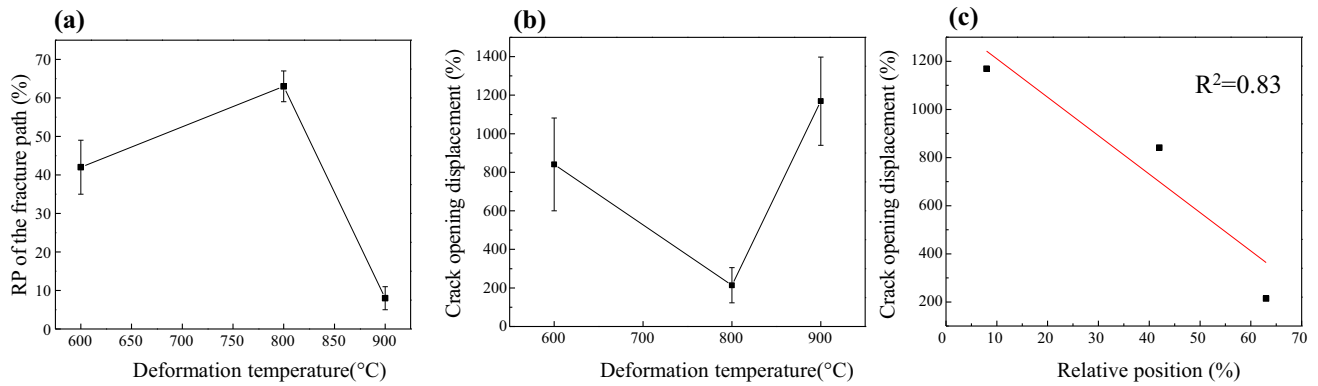
Figure 14 **a** The relative position (RP) of the fracture path in DAZ; **b** Average crack opening Displacement; **c** Scatter chart showing the relationship of the relative position and the average COD.
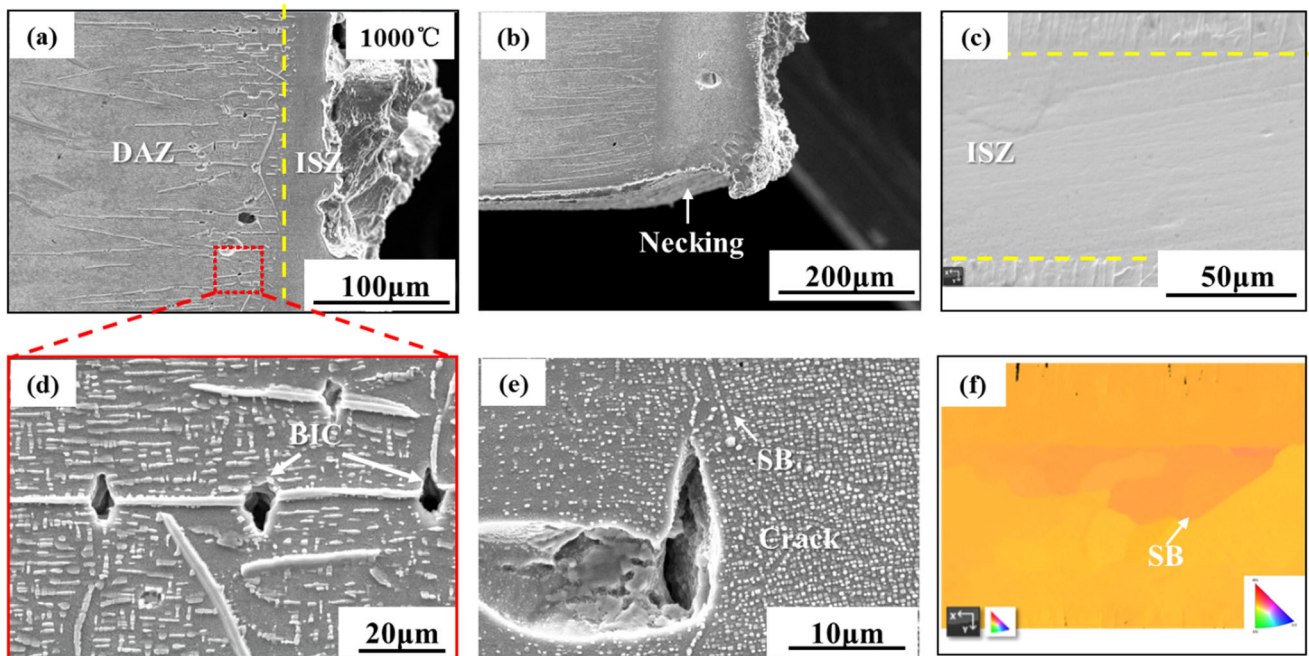

Figure 15 Microstructure of the longitudinal-section after tensile to fracture test at 1000 °C and EBSD surface-scanning test results of the ISZ. **a** Morphology of the fracture path; **b** Morphology of the margin of the fracture; **c**, **f** EBSD result; **d** Enlarged image of the DAZ; **e** Crack in the ISZ.

Discussion

Temperature dependence of deformation mechanisms

Based on the experimental results, it can be found that from RT to 1000 °C, the variation trend of the deformation mechanism is basically the same, namely from the dislocation shearing to bypassing the γ′ phase. However, at a certain temperature, the deformation mechanism of different joint areas may

be different. In the face-centered cubic crystal, the a/2 <110> dislocation is the most stable, and the close-packed plane is (111), so the movement of the a/2 <110> dislocations on the (111) plane in the γ channel is favorable [28]. We found three types of interactions between the a/2 <110> dislocation and the γ′ phase, namely the a/2 <011> dislocation pairs shearing the γ′ phases, which can prevent the increase of APB energy of the system; the a/3 <112> partial dislocations shearing the γ′ phases, which would leave some SFs in the γ′ phases;

Figure 16 SEM images of the fracture surfaces of the TLP joints tested at **a** 600 °C, **b** 800 °C, and **c** 900 °C.
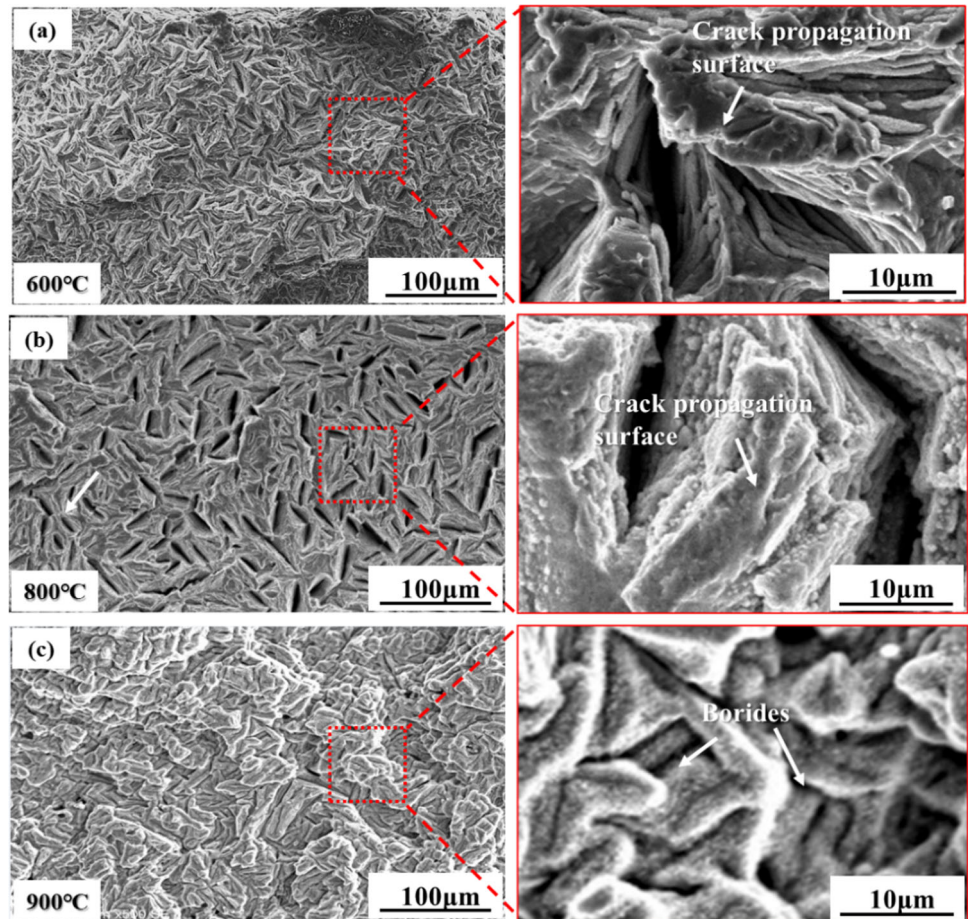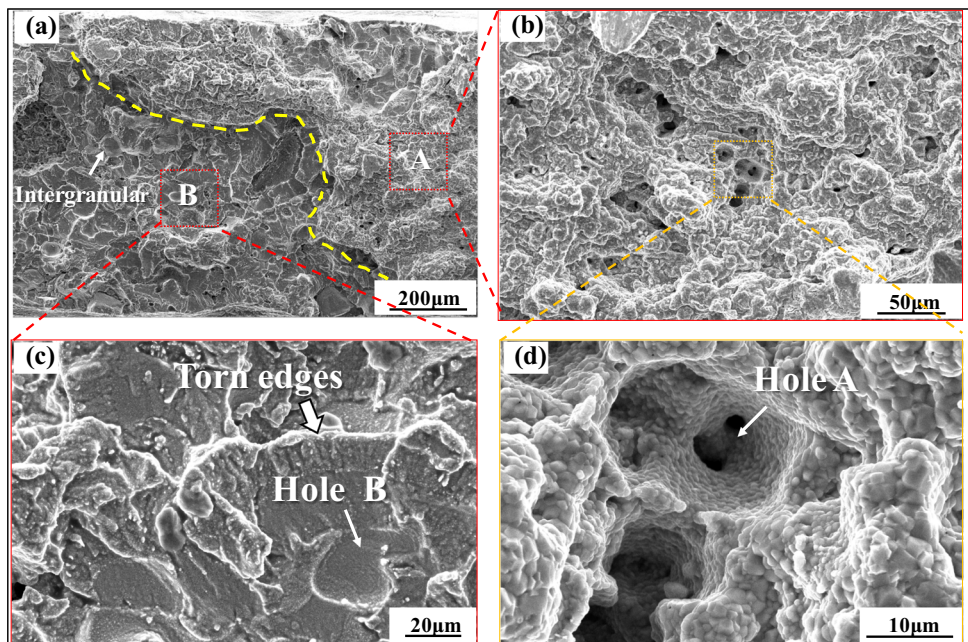

Figure 17 SEM images of the fracture surface tested at 1000 °C. **a** Macro morphology of the fracture surface; **b** Microstructure of area A; **c** Microstructure of area B; **d** Partial enlarged image showing the morphology of Hole A.

bypassing the γ' phase. For the first condition, the required critical shear stress (CSS) could be calculated using the following equation [29]

$$\tau_{c-\mathrm{APB}} = 1.02 \frac{G \cdot b \cdot w \cdot f1/2}{\pi d} \left(\frac{\pi d \cdot \gamma_{\mathrm{APB}}}{w \cdot G \cdot b^2} \right)^{1/2} \left(1 + \frac{C \cdot f1/2}{2} \right) \tag{1}$$

For the second condition [29]:

$$\tau_{c-\mathrm{SF}} = \sqrt{3} \left(\frac{G(2-v)}{12(1-v)} \cdot \frac{\pi b}{2d} + \frac{2\gamma\mathrm{SF}}{3b} \right) \tag{2}$$

For the bypassing of dislocation, the required stress could be expressed as follows [28]:

$$\tau_{c-\mathrm{BP}} = \frac{G \cdot b}{l} \tag{3}$$

For the <001> applied stress, the critical resolved shear stress (CRSS) could be calculated using the following equation [30]:

$$\tau_{\mathrm{exp}} = m \cdot \sigma_{\mathrm{app}} \tag{4}$$

In the above equations, the $\tau_{c\text{-APB}}$ and $\tau_{c\text{-APB}}$ are the CSSs required for a/2 <011> dislocation pairs shearing and a/3 <112> partial dislocations shearing, respectively; $\tau_{c\text{-BP}}$ is the required stress for dislocation bypassing; τ_{exp} is the CRSS; G is the shear modulus, which can be acquired by the stress–strain curve ($88.3 \sim 69.6$ GPa); v is the Poisson ratio ($v = 0.356$ [31]); b is the Burgers vector ($b = 0.25$ nm); w is a dimensionless constant, which represents the degree of elastic repulsion between the strongly coupled dislocation pairs ($w = 2.8$ [32]); f is the volume fraction of γ' phase (according to Ref [22]); l is the distance between the γ' phases; c is a constant ($c = 1$ [32]); σ_{app} is the applied stress (yielding strength); m is the Schmid factor

($m = 0.408$ [28]); γ_{APB} and γ_{SF} are the APB and SF energies, respectively. As for the APB energy, it is widely accepted that it decreases with temperature. The decreasing rate increases significantly when the temperature is close to the solid solution temperature of the γ' phase [33]. At the same time, the composition of the ISZ is closer to a NiCo-based alloy [30], and the APB energy increases as the γ' composition transfers toward Co-based alloys. Therefore, the APB energy of ISZ is assumed to be $86 \sim 134$ mJm^{-2}, and that of BM is $135 \sim 175$ mJm^{-2} [34]. The SF energy shows a monotonic increase from the Ni-based to Co-based alloys [30]. According to Refs [30, 35], the SF energy of ISZ is assumed to be $10 \sim 35$ mJm^{-2}, and that of BM is assumed to be $35 \sim 50$ mJm^{-2}. Thus, based on Eqs. (1) $\sim$ (4), the required critical stresses for different types of interactions between the a/2 <110> dislocation and the γ' phase are illustrated in Fig. 18.

In the temperature range of RT $\sim$ 600 °C, the CRSS of the ISZ is higher than all the required stresses, so the simultaneous occurrence of the three interactions should be expected. However, the CSS of APB is relatively lower (Fig. 18a), so the coupled dislocation pairs shearing the γ' phases in the ISZ is preferred to occur in the loading process. The shearing of the first dislocation pair can reduce the effective diameter of the γ' phase, which makes it easier for the second dislocation pair to move on the same plane [36]. Therefore, the strongly coupled a/2 <011> dislocations shearing the γ' phases should be the dominant deformation mechanism in the ISZ, and the localized deformation mode is favored. In the same way, the CSS of SF is relatively lower (Fig. 17b), and the a/3 <112> partial dislocations shearing the γ' phases should be the dominant deformation mechanism in the BM. The extremely heterogeneous slip

Figure 18 Variations of the critical resolved shear stress (CRSS), critical shear stress (CSS), and the required stress for dislocation bypassing the γ' phase with temperature. **a** ISZ; **b** BM.
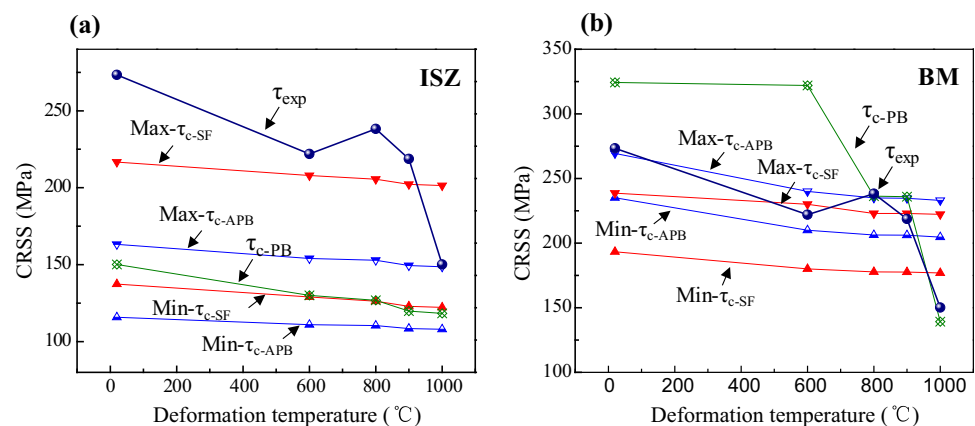
lines observed in the ISZ and BM (see Fig. 12) should further prove this view. Thus, one deformation mechanism should dominate the deformation in the low-temperature range. Besides, the deformation of the ISZ is relatively small compared with that of the BM. The reason is related to the large amount of S-γ′ phases in the γ channel. Our previous results have proved a higher proportion of the S-γ′ phases can greatly strengthen the ISZ and make the ISZ has a higher microhardness [22]. At 600 °C, according to the morphology of the S-γ′ phases and their internal dislocation configuration (Fig. 8b), the dislocations can still shear the S-γ′ phases. This indicates that the S-γ′ phases did not dissolve at this temperature. Therefore, they can still play a role in strengthening the ISZ and making the ISZ has a higher strength. Based on this analysis, we simulated the stress field of the joint in the low-temperature range by finite element analysis (Fig. 19a and c); the result shows more deformation has occurred in the BM than in the ISZ and the macro-morphology of the joint is consistent with the fact (see Figs. 19c and 12a), which can further prove our inference.

At 800 °C ∼ 900 °C, the S-γ′ phases in the ISZ begin to dissolve, and the dislocation bypassing resistance decreases, and the Orowan bypassing mechanism begins to work, which makes it difficult for a second dislocation to follow on the same glide plane. Thus, the deformation mode should become less localized. Meanwhile, the CRSS of the ISZ is still higher than all the required stresses (Fig. 18a), and a mixed deformation mechanism of dislocations shearing and bypassing the γ′ phases could be expected. Besides, more SFs can be observed at 800 °C (Fig. 9a ∼ b), which should attribute to the decrease of SF energy [37]. At 900 °C, the SFs can rarely be observed (Fig. 10a ∼ b). This indicates that the SF energy increases when the temperature is over 800 °C. Different from the ISZ, the required stress for dislocation bypassing the γ′ phase in the BM is still relatively larger and the CSS for SF is lower at this temperature range (Fig. 18b), so $a/3$ <112> partial dislocations shearing the γ′ phases still dominates the deformation. However, an abnormal yield behavior occurred at 800 °C (Fig. 6b). Such behavior is generally believed to be caused by the formation of Kear–Wilsdorf block (K–W block) [24], which can also make the deformation less localized and the work-hardening become severe (Fig. 6a).

At 1000 °C, no SFs can be observed in the γ′ phases of ISZ and BM, which indicates that the decomposition of $a/2$ <101> total dislocations is not the optimum deformation mechanism. Instead, the partially dissolved γ′ phases in the ISZ and BM make a wider γ channel and give rise to the dislocation bypassing deformation. Meanwhile, the APB energy could decrease dramatically, which leads to some $a/2$ <110> dislocations cut into γ′ phases directly, and leaves the APBs in the γ′ phases (Fig. 11). As the S-γ′ phases in the ISZ are totally dissolved, the ISZ should become soft, and more deformation would occur. The simulated results can prove this view (Fig. 19e ∼ h), which are consistent with the fact (Fig. 15b). Besides, some dislocation nets can be observed at the γ/γ interface, which is easy to form during the high-temperature and low-stress creep process [38]. The formation time usually takes at least several hours. However, the tensile process lasted only a few minutes. According to Ref. [39], in addition to temperature, stress can also affect the formation rate of the dislocation net. The flow stress used in this test is much higher than the commonly used creep stress. Therefore, the higher flow stress could accelerate the formation process. Besides, as the loading time is short, it is almost impossible to form the regular dislocation nets (Fig. 11a). The dislocation net is conducive to preventing subsequent dislocation from shearing the γ′ phase, which is beneficial for strengthening the alloy. However, dislocations plug at high temperature may lead to dislocations climbing and form vacancy defects. The high-frequency appearance of the wavy dislocations (Fig. 11a) can further prove this view.

The deformation mechanism of the DAZ is relatively complex because it contains many borides and the γ′ phase is not uniformly distributed. The composition of the γ/γ′ in DAZ is closer to that in BM, so the deformation mechanism should be similar to that of the BM at different temperature ranges. According to Fig. 19, the stress distribution is extremely uneven in the DAZ, and the stress around the borides is relatively lower, which can explain why the dislocation density there is always lower. However, when the borides break, the stress around the BIC increases instantaneously, which is higher than that of the BM (Fig. 19b and d). Therefore, the three types of interaction between the dislocation and γ′ could happen simultaneously at medium and low temperatures (Figs. 7, 8, 9 and 10). However, at high temperature,
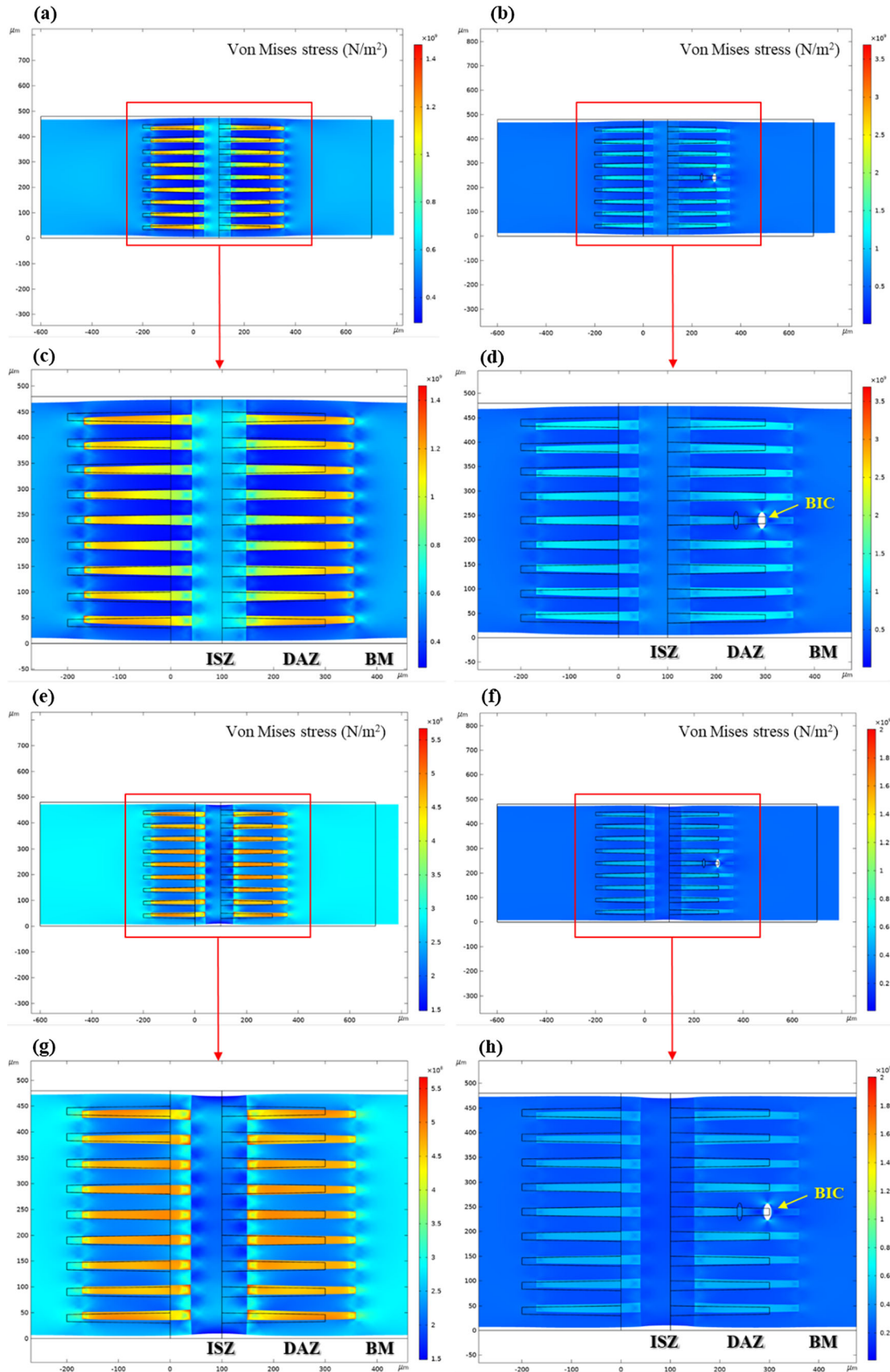
◀**Figure 19** Finite element analysis of the stress field of the TLP joint under tensile stress. **a∼d** Low temperature; **a∼d** High temperature; **a**, **c**, **e**, and **f** illustrate the perfect joints; **b**, **d**, **f**, and **h** illustrate the joints with the BICs; **c**, **d**, **g**, and **h** are the partial enlarged images of **a**, **b**, **e**, and **f**, respectively.

the stress distribution becomes more uniform (Fig. 19f and h), so the deformation mechanism should be much closer to the BM.

Temperature dependence of fracture mechanism and fracture path

This study presents a temperature dependence of the fracture mechanism. At RT, the fracture occurs at the BM, so we only discuss the fracture mechanism at 600 °C∼1000 °C. As the results indicate the fracture occurs at DAZ from 600 °C to 900 °C, and many BICs can be observed (Fig. 13), together with the fracture morphologies (Fig. 16), it can be judged the coalescence of the BICs leads to the fracture of the joint at this temperature range. At 1000 °C, more deformation has occurred in the DAZ, the movement of dislocations at the sub-grain boundaries and the γ′ phases would be hindered, which leads to the cracks at the sub-grain boundaries. Simultaneously, the hindered dislocations can also move by climbing, leaving some vacancy defects on the boundary. The accumulation of some vacancies forms the microhole. Therefore, the fracture mechanism belongs to the coalescence of the micro-holes and the SB-induced cracks.

This study also presents a temperature dependence of the location of the fracture path, which shifts from BM to ISZ as the deformation temperature increases (Figs. 13 and 15). In the tensile tests of welding specimens, fracture at the BM in the low-temperature regime is not an unusual phenomenon, simply because of utilizing the filler metal with higher strength. This proves the prepared TLP joint can get a higher strength than the BM at RT.

In the temperature range of 600 °C∼900 °C, we found a regular temperature dependence of the fracture location (see Fig. 14a). Such behavior should be determined by the uneven internal structure of the DAZ. According to Fig. 18, the stress on the boride is much higher than the matrix, and the stress is higher near the DAZ/BM interface. Therefore, the borides near the interface are preferred to break, which is

consistent with the in situ observation of the BIC [40]. According to Ref. [40], the BICs diffuse to the ISZ direction in the loading process, where the content of boride is higher. Thus, the diffusion can increase the coalescence possibility of the BICs because the borides become closer to each other in the diffusion direction. As the crack propagation is related to the toughness of the matrix, the lower the toughness of the matrix, the easier the cracks are connected. Therefore, when the toughness of the matrix is low, it does not need a large crack-extension distance for the BICs to connect, which means the fracture would occur at the position where the content of boride is relatively larger and vice versa. As the abnormal yield behavior happens at 800 °C, the toughness of the matrix at this temperature should be lower. The statistic result of the CODs (Fig. 13b) can further prove this view, which is an indicator of the toughness [28]. Thus, it is easier to understand that the relative position of the fracture path first increases and then decreases from 600 °C∼900 °C (Fig. 13a).

At 1000 °C, the strength of the matrix decreases again, the propagation of BICs requires higher energy, which is why the tips of the BICs become blunt (Fig. 14d). Therefore, although the loading induces many BICs, they do not lead to the fracture of the joint. By contrast, most sub-grain boundaries are vertical to the loading direction, inducing some large-scale cracks. Thus, it can be speculated that the cracks growth rate in ISZ exceeds that in DAZ, making the fracture path locates at ISZ.

The present study indicates that the DAZ precipitates can lead to the low-medium temperature brittleness of the TLP joint, which can affect the tensile property at a relatively large temperature range. To further improve the mechanical property, application of a proper PBHT to dissolve the boride phases in DAZ is necessary, and some reverent studies successfully achieved an ideal joint by using the PBHT [41–43],

Conclusion

1. At low temperature, the deformation of the TLP joint is heterogeneous. The deformation mechanism is mainly dislocation shearing the γ′. As deformation temperature increases, the deformation is gradually transferred from the BM to the joint, and the deformation becomes uniform. The deformation mechanism gradually transfers to Orowan bypassing

mechanism. The difference of deformation mechanism in each region of the joint is the competition result of various energies.

2. The DAZ boride can strengthen the joint at low temperature, but it induces cracks at medium temperature, which leads to the brittle fracture. The fracture position changes from BM to DAZ, and finally to ISZ with the increase in deformation temperature.

3. Dissolving the secondary-γ' in the bonding area is the essence of being a weaker TLP joint at high temperature. More γ'-forming elements are suggested to add to the filler alloy to increase the volume fraction of the joint, which can increase its intrinsic strength. Besides, sub-grains in the TLP joint should be reduced as low as possible, which can greatly reduce the high-temperature properties of a TLP joint.

Data Availability

The data used to support the findings of this study are available from the corresponding author upon request.

Declarations

Conflict of interest We declare that we have no known competing financial interests or personal relationships that could have appeared to influence the work reported in this paper.

References

[1] Sato J, Omori T, Oikawa K, Ohnuma I, Kainuma R, Ishida K (2006) Cobalt-base high-temperature alloys. Science 312(5770):90–91

[2] Xue F, Zenk CH, Freund LP, Hoelzel M, Neumeier S, Goken M (2018) Double minimum creep in the rafting regime of a single-crystal Co-base superalloy. Scripta Mater 142:129–132

[3] Lu S, Antonov S, Li L, Liu C, Feng Q (2020) Atomic structure and elemental segregation behavior of creep defects in a Co-Al-W-based single crystal superalloys under high temperature and low stress. Acta Mater 190:16–28

[4] Freund LP, Messe OM, Barnard JS, Goken M, Neumeier S, Rae CMF (2017) Segregation assisted microtwinning during creep of a polycrystalline L1(2)-hardened Co-base superalloy. Acta Mater 123:295–304

[5] Wen MY, Sun Y, Yu JJ, Meng J, Wang SY, Dong ZG, Niu JT, Sun XF, Zhou YZ (2021) Enhancement of multi-pass weld-crack resistance of Co-based superalloys by B-doping 182:111527

[6] Mattheij JHG (1985) Role of brazing in repair of superalloy components advantages and limitations. Mater Sci Tech-Lond 1(8):608–612

[7] Pouranvari M (2009) Diffusion brazing of a precipitation hardened nickel based superalloy, metal 2009, conference proceedings, pp 574–579

[8] Duvall DS, Owczarski WA, Paulonis DF (1974) TLP bonding: a new method for joining heat resistant alloys. Welding J 20(4):203–213

[9] Pouranvari M (2009) Solidification behavior during diffusion brazing of a nickel based superalloy, metal 2009, conference proceedings, pp 580–583

[10] Pouranvari M, Ekrami A, Kokabi AH (2013) Solidification and solid state phenomena during TLP bonding of IN718 superalloy using Ni-Si-B ternary filler alloy. J Alloy Compd 563:143–149

[11] Binesh B, Gharehbagh AJ (2016) Transient liquid phase bonding of IN738LC/MBF-15/IN738LC: solidification behavior and mechanical properties. J Mater Sci Technol 32(11):1137–1151

[12] Wang GL, Sun Y, Wang XG, Liu JD, Liu JL, Li JG, Yu JJ, Zhou YZ, Jin T, Sun XD, Sun XF (2017) Microstructure evolution and mechanical behavior of Ni-based single crystal superalloy joint brazed with mixed powder at elevated temperature. J Mater Sci Technol 33(10):1219–1226

[13] Arhami F, Mirsalehi SE (2018) Microstructural evolution and mechanical properties evaluation of IN-939 bonds made by isothermal solidification of a liquated Ni–Cr–B interlayer. Metall Mater Trans A 49a(12):6197–6214

[14] Doroudi A, Shamsipur A, Omidvar H, Vatanara M (2019) Effect of transient liquid phase bonding time on the microstructure, isothermal solidification completion and the mechanical properties during bonding of Inconel 625 superalloy using Cr-Si-B-Ni filler metal. J Manuf Process 38:235–243

[15] Wang SY, Sun Y, Hou XY, Cui CY, Sun XF, Zhou YZ (2019) Borides of preferred orientation formed in the transient liquid phase joint of γ′-strengthened Co-base single crystal superalloy. Mater Lett 246:190–194

[16] Hu XB, Zhu YL, Shao XH, Niu HY, Zhou LZ, Ma XL (2015) Atomic configurations of various kinds of structural intergrowth in the polytypic M_2B-type boride precipitated in the Ni-based superalloy. Acta Mater 100:64–72

[17] Zhang BQ, Sheng GM, Jiao YJ, Gao ZH, Gong XF, Fan H, Zhong J (2017) Precipitation and evolution of boride in diffusion affected zone of TLP joint of Mar-M247 superalloy. J Alloy Compd 695:3202–3210

[18] Arhami F, Mirsalehi SE, Sadeghian A (2019) Effect of bonding time on microstructure and mechanical properties of diffusion brazed IN-939. J Mater Process Tech 265:219–229

[19] Doroudi A, Pilehrood AE, Mohebinia M, Dastgheib A, Omidvar H (2020) Effect of the isothermal solidification completion on the mechanical properties of Inconel 625 transient liquid phase bond by changing bonding temperature. J Market Res 9(5):10355–10365

[20] Amiri D, Sajjadi SA, Bakhtiari R, Kamyabi-Gol A (2018) The role of TLP process variables in improvement of microstructure and mechanical properties in TLP joints of GTD-111/Ni-Cr-Fe-B-Si/GTD-111 system. J Manuf Process 32(APR.):644–655

[21] Phillips AL (1957) Welding handbook, welding handbook

[22] Wang SY, Sun Y, Hou XY, Cui CY, Sun XF, Zhou YZ (2020) Investigation on microstructure and mechanical properties of a vacuum brazed joint of γ′-strengthened Co-based single crystal superalloy before and after the post-bond heat treatment. Vacuum 177:109413

[23] Shi L, Yu JJ, Cui CY, Sun XF (2015) Effect of Ta additions on microstructure and mechanical properties of a single-crystal Co-Al-W-base alloy. Mater Lett 149:58–61

[24] Shi L, Yu JJ, Cui CY, Sun XF (2015) Temperature dependence of deformation behavior in a Co-Al-W-base single crystal superalloy. Mat Sci Eng A Struct 620:36–43

[25] Milligan WW, Antolovich SD (1991) The mechanisms and temperature dependence of superlattice stacking fault formation in the single-crystal superalloy PWA 1480. Metall Trans A 22:2309–2318

[26] Wang XG, Liu JL, Jin T, Sun XF, Zhou YZ, Hu ZQ, Do JH, Choi BG, Kim IS, Jo CY (2015) Deformation mechanisms of a nickel-based single-crystal superalloy during low-cycle fatigue at different temperatures. Scripta Mater 99:57–60

[27] Zhang JX, Harada H, Koizumi Y, Kobayashi T (2010) Dislocation motion in the early stages of high-temperature low-stress creep in a single-crystal superalloy with a small lattice misfit. J Mater Sci 45(2):523–532

[28] Meyers M (2009) Mechanical behavior of materials (2nd edn), vol 81, no 2. Aircraft Eng & Aerospace Tech

[29] Yuan Y, Zhu B, Song RH, Yang GX, Shen L (2017) Tensile deformation mechanisms at various temperatures in a new directionally solidified Ni-base superalloy. J Alloys Comp Interdisc J Mater Sci Solid State Chem Phys 694:502–509

[30] Titus MS, Eggeler YM, Suzuki A, Pollock TM (2015) Creep-induced planar defects in $L1_2$-containing Co- and CoNi-base single-crystal superalloys. Acta Mater 82:530–539

[31] Feller-Kniepmeier M, Link T, Poschmann I (1996) Temperature dependence of deformation mechanisms in a single crystal nickel-base alloy with high volume fraction of γ′ phase. Acta Mater 44(6):2397–2407

[32] Reppich B (1982) Some new aspects concerning particle hardening mechanisms in γ' precipitating Ni-base alloys—I. Theoretical concept. Acta Metall Mater 30(1):87–94

[33] Kruml T, Viguier B, Bonneville J, Martin JL (1997) Temperature dependence of dislocation microstructure in $Ni_3(Al, Hf)$. Mater Sci Eng, A 234–236:755–757

[34] Okamoto NL (2011) Plastic deformation of polycrystals of $Co_3(Al, W)$ with the L12 structure. Phil Mag 91(28):3667–3684

[35] Zhang P, Yuan Y, Shen SC, Li B, Zhu RH, Yang GX, Song XL (2017) Tensile deformation mechanisms at various temperatures in a new directionally solidified Ni-base superalloy. J Alloy Compd 694:502–509

[36] Grant B, Francis EM, Fonseca J, Daymond MR, Preuss M (2012) Deformation behaviour of an advanced nickel-based superalloy studied by neutron diffraction and electron microscopy. Acta Mater 60(19):6829–6841

[37] Yuan Y, Gu YF, Osada T, Zhong ZH, Yokokawa T, Harada H (2012) Deformation mechanisms in a new disc superalloy at low and intermediate temperatures. Scripta Mater 67(2):137–140

[38] Tan XP, Liu JL, Jin T, Hu ZQ, Hong HU, Choi BG, Kim IS, Jo CY, Mangelinck D (2013) Effect of Ru additions on very high temperature creep properties of a single crystal Ni-based superalloy. Mater Sci Eng A Struct Mater Prop Microstruct Process 580(10):21–35

[39] Field RD, Pollock TM, Murphy WH (1992) The development of γ/γ' interfacial dislocation networks during creep in Ni-base Superalloy. Superalloys 557–566

[40] Wang SY, Sun Y, Hou XY, Cui CY, Sun XF, Zhou YZ (2020) Fracture mechanism of transient liquid phase bonding joint of γ'-strengthened Co-based single crystal superalloy. Mater Lett 258:126730

[41] Wang SY, Sun Y, Cui CY, Sun XF, Zhou YZ, Ma YM, An HL (2021) Effect of post-bond heat treatment on the microstructure and high temperature mechanical property of a TLP bonded γ'-strengthened Co-based single crystal superalloy. J Mater Sci Technol 80(4):244–258

[42] Danesh A, Ata K-G, Seyed Abdolkarim S (2022) Standard heat treatment effects on TLP bonded IN-738LC superalloy using BNi-9 filler: an approach to make an ideal joint. Trans Nonferr Metals Soc China 32(01):192–205

[43] Sun W, Li X, Chen M, Ding R, Qiao Z, Wang Z, Liu C, Liu Y (2022) Effect of post bonding heat treatment on the local strain evolution of transient liquid phase bonded RAFM steel. Mater Sci Eng, A 840(04):143008

Publisher's Note Springer Nature remains neutral with regard to jurisdictional claims in published maps and institutional affiliations.